Additive Manufacturing 63 (2023) 103418

Contents lists available at ScienceDirect

Additive Manufacturing

journal homepage: www.elsevier.com/locate/addma

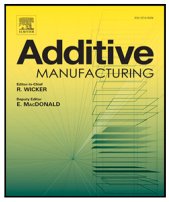

Research paper

Design, manufacturing and testing of 3D printed variable-stiffness laminates for improved open-hole tensile behaviour

M. Iragi [a,*], C. Pascual-González [b,c], A. Esnaola [a], U. Morales [a], J. Aurrekoetxea [a], C.S. Lopes [b,d], L. Aretxabaleta [a]

[a] Mondragon Unibertsitatea, C/Loramendi 4, 20500, Arrasate-Mondragon, Spain
[b] IMDEA Materials Institute, C/Eric Kandel 2, 28906, Getafe, Madrid, Spain
[c] Materials Science and Engineering Area, Rey Juan Carlos University, C/Tulipán s/n, 28933, Móstoles, Madrid, Spain
[d] Luxembourg Institute of Science and Technology, 5, avenue des Hauts-Fourneaux, L-4362 Esch-sur-Alzette, Luxembourg

ARTICLE INFO

Keywords:
Material extrusion
Continuous fibre-reinforced polymers
Fibre-steering
Variable-stiffness
Open-hole

ABSTRACT

Using 3D printing, continuous fibre can be steered in high curvature paths to create variable-stiffness (VS) laminates for applications such as notched laminates. In the present study, VS 3D printed continuous carbon fibre-reinforced thermoplastic laminates were designed, manufactured, and tested, to improve open-hole tensile behaviour. The design was carried out taking into account the current limitations of fused filament fabrication. A curvilinear function was used to describe the fibre trajectory of the VS laminates, which enabled the parametrisation of the design-oriented meso-scale model based on the finite element method. Conventional stress-based models for the estimation of damage initiation and ultimate failure strengths were adapted to the behaviour of the 3D printed material. These models successfully reproduced the fibre-dominated behaviour of the printed laminate. An as-manufactured model was also developed to analyse the effect of defects caused by manufacturing constraints. VS laminates presented higher strength than quasi-isotropic reference laminates for holes larger than ∅1 mm, increasing to more than 30% for holes of ∅6 mm or larger. In addition, this increase in strength combined with the slight decrease in stiffness significantly increased the energy absorbed up to failure (up to 200%).

1. Introduction

Fibre-steering has expanded the design space for composite laminates, particularly in the development of high performance and light weight components, and has become the subject of considerable research in recent decades [1]. The stiffness in these non-conventional laminates is tailored to create a more favourable load distribution. As a result, laminates with different stiffness depending on the spatial location can be designed. Known as variable-stiffness (VS) laminates, these take full advantage of the directional properties of composite materials and improve component performance over conventional straight-fibre, or constant-stiffness (CS) laminates. This improvement has been demonstrated for different criteria such as stiffness, strength, dynamic behaviour, and buckling [2].

Two main approaches have been proposed to model and optimise the behaviour of VS laminates: laminate stiffness discretisation and fibre path parametrisation [3]. In the first, independent stiffness properties caused by fibre orientations are determined for discrete regions of the laminate, such as the elements in finite element modelling. Hyer and Lee [4] pioneered the application of this model to improve the buckling resistance of composite plates with central circular holes. This approach has since been widely used to determine fibre trajectories, such as principal stress and load paths. The second strategy uses a curvilinear function to describe the trajectory of the fibre. First introduced by Gürdal and Olmedo [5], in this approach the fibre orientation angle varies linearly with position. These structures are referred to as VS panels and were the basis for many later developments, mainly because of their manufacturability. Most notably, Lopes et al. analysed the progressive damage and failure of VS panels [6] and designed structures tolerant to stress concentrations around large cut-outs [1].

The application of fibre-steering has gone hand in hand with technological development [7]. In recent years, automatic manufacturing technologies such as Automated Fibre Placement (AFP) have been developed to produce high performance large-scale VS panels for the

* Corresponding author.
E-mail address: miragi@mondragon.edu (M. Iragi).

https://doi.org/10.1016/j.addma.2023.103418
Received 10 May 2022; Received in revised form 2 January 2023; Accepted 16 January 2023
Available online 18 January 2023

aerospace industry. However, the constraints imposed by this technology (e.g., minimum steering radius of about 500 mm), the defects produced during manufacture (gaps or overlaps) [8], and high manufacturing costs have hampered the wider use of VS laminates.

3D printing is a more recently developed additive manufacturing technology for fibre-reinforced plastic components. This technology is attracting widespread interest because of the design freedom it offers to create complex products in terms of material, structure, and function [9,10]. Multi-scale architected composites can be developed with this technology: (1) topology optimisation at the macro-scale, (2) continuous fibre path design and cellular/lattice structure design at the meso-scale, and (3) control of constituents at the micro-structural level to obtain, for example, functionally graded composites. In addition, 3D printing requires fewer steps than conventional manufacturing techniques, with no special tools and little waste. The research of Morales et al. [11,12] showcases the potential of this new technology, in which thin-walled profiles with promising crush behaviour for crashworthiness applications were printed and tested.

Despite this potential, continuous fibre 3D printing is at an early stage of development and has limitations that restrict its use in real applications. On the one hand, the mechanical properties of printed composites are lower than those obtained by conventional manufacturing methods, due to the presence of more defects and a lower fibre volume fraction [13]. With regard to manufacturing, free fibre path planning printers are not yet commercially available, and because of low production capacity and medium print volumes, this technology cannot currently be used for mass production. On the other hand, accurate models to reproduce the behaviour of these non-conventional materials and structures are yet to be developed, mainly because they are highly heterogeneous and anisotropic. It is therefore necessary to adapt existing models and analysis tools, or create new ones, to design reliable high-performance components.

Material extrusion, known as Fused Deposition Modelling (FDM) or Fused Filament Fabrication (FFF), is currently the most widely used composite 3D printing process due to its simplicity and performance [14]. In FFF, a fibre-reinforced thermoplastic filament, usually pre-impregnated, is melted and extruded through a nozzle and deposited on the printing layer. This allows greater fibre curvature freedom and a thinner fibre-path width than the AFP process. FFF 3D printing of continuous fibre composites is thus ideally suited to enlarge the design and manufacturing spaces of steered-fibre composites to include, for example, structurally-critical notches and fastening holes.

In line with this idea, several 3D printing solutions for open-hole tensile (OHT) cases have recently been developed [15–24]. In these works, different fibre trajectories are proposed, such as: principal stress [15], load path [16,17,23], fluid flow streamlines [19,20], hole contour [21,22], and others resulting from numerical optimisation processes [18,19]. As a result, a load redistribution is achieved that increases component stiffness [17,19,24], reduces stress concentration [15,21] and significantly increases the ultimate strength [15,17–20,22–24]. Despite these preliminary studies, the application of 3D printing technology to the fabrication of non-conventional laminates in terms of manufacturing, modelling, and design has yet to be explored. This motivated the present design and testing program, where fibre-steering by means of 3D printing is investigated to tailor stiffness and improve the strength of notched composites.

The aim of the present study therefore, is to evaluate the capacity of continuous fibre 3D printing for the manufacture of variable-stiffness laminates that enhance the mechanical performance of structural components. To this end, we designed, manufactured, and tested variable-stiffness OHT specimens and compared their behaviour with a constant-stiffness quasi-isotropic (QI) reference laminate for different hole sizes. The specimens were manufactured on a commercial FFF printer to assess the current capabilities and limitations of the process. A curvilinear function was used to describe the fibre trajectory of the VS laminates, which allowed the design models to be parameterised. Conventional stress-based models were employed for the design of the VS laminates. These estimated the OHT loads at which damage initiation and ultimate failure occur and were adapted to the 3D printed material behaviour. Finally, the most promising laminates were manufactured and tested, and the influence of manufacturing constraints and defects was analysed.

2. 3D printing of variable-stiffness laminates

2.1. Technology and material

In this study, we used the FFF 3D printing technology of pre-impregnated filament from Markforged® [25]. Continuous carbon fibre reinforced polyamide (cCF/PA) was selected due to its higher strength and stiffness as compared to the other materials available for this technology [26]. The micro-structure, composition, and mechanical behaviour of cCF/PA were analysed and reported in previous works [13,27,28]. Calorimetric test results indicated that the PA matrix is amorphous with a glass transition temperature of 143 °C [27]. The fibre volume fraction in the printed samples was 31.4%, while the voids, located mainly at bead and layer limits, were 7.5% in volume [13]. The mechanical behaviour in the longitudinal direction was found to be satisfactory, however the mechanical performance under transverse and interlaminar loads was highly influenced by manufacturing defects (non-homogeneous fibre distribution, large amounts of intra- and inter-laminar voids, and weak interlayer bonding) [13,28]. These defects can be considerably reduced by applying post-processing heat treatments without modifying the nominal dimensions of the printed part, as reported by Pascual-González et al. [29]. The elastic and strength properties at ply level and the interlaminar fracture toughness of the printed cCF/PA material are shown in Table 1.

Markforged® provides software, called Eiger™, for print setup. This technology is a closed solution and offers limited strategies for layer filling: isotropic filling and concentric filling. The isotropic pattern fills the layer with straight and parallel beads, creating a unidirectional layer similar to traditional laminated composites. In concentric filling, the fibre path follows the outer contour of the part, tracing a spiral from outside to inside with a given number of rings. In this study, isotropic filling was used to print the straight-fibre layers (0°, 45°, and 90°), while concentric filling was used to print the steered-fibre layers. Eiger™ also includes bottom and top layers (called floor and roof, respectively) to protect the part. These layers are 100% filled with a ±45° rectangular pattern of Onyx™ and cannot be omitted. Onyx™ is a polyamide 6 reinforced with carbon micro-fibres, a material available in the Mark Two™ printer for construction and filling.

Using this technology, curvature radii of up to 1 mm can be produced, although radii of less than 15 mm are not recommended to prevent twisting and fibre breakage [30,31]. The minimum cutting length is approximately 50 mm, which corresponds to the minimum printable bead length. During the process, the 380 μm diameter filament is flattened to a bead width of approximately 0.9 mm and a thickness of 125 μm (thickness of the printed layer).

2.2. Design for manufacturing

In this study, the commonly adopted fibre orientation definition of Gürdal and Olmedo [5] was employed. The orientation angle $\theta(y)$ of the reference fibre path varies linearly with respect to the y-position, from T_0 at the centre of the width W of the specimen to T_1 at the free edge (Fig. 1(a) and Eq. (1)). The path of the fibre is considered antisymmetric with respect to the origin, and the ideal steered-fibre layer is created by shifting the reference path along the x-axis direction. Thus, the orientation of each layer is defined with only two parameters (T_0 and T_1), making it suitable for parametric and optimisation studies. This steered-fibre layer configuration is referred to as $\langle T_0|T_1\rangle$,

Table 1
Mechanical properties of the printed cCF/PA material [13,28].

Ply elastic properties	E_{11} = 69.4 GPa; E_{22} = 3.5 GPa; ν_{12} = 0.41; G_{12} = 1.9 GPa
Ply strengths (MPa)	X_T = 905.3; X_C = 426.0; Y_T = 17.9; Y_C = 66.0; S_L = 43.4
Interlaminar fracture toughness (J/m^2)	G_{Ic} = 1260; G_{IIc} = 1180

Table 2
Layup characteristics of the designed and tested QI and VS laminates.

Laminate	Designation	Ply orientation (°)	Ply ratios (%)	Stacking sequence
Quasi-isotropic	QI	0/±45/90	25/50/25	$[-45/0/45/90]_{2s}$
Variable-stiffness	VS$\langle T_0\|T_1\rangle$	$\pm\langle T_0\|T_1\rangle$/±45/90	50/25/25	$[-45/+\langle T_0\|T_1\rangle/-\langle T_0\|T_1\rangle/90/45/-\langle T_0\|T_1\rangle/+\langle T_0\|T_1\rangle/90]_s$

and is usually combined with layers containing equal but opposite orientations $\pm\langle T_0|T_1\rangle$.

$$\theta(y) = \frac{2(T_1 - T_0)}{W} y + T_0 \tag{1}$$

The manufacturing constraints of current 3D printing technology in fibre-steering (Section 2.1) require that VS laminates are designed taking into consideration the manufacturing process. In the present paper, the required fibre trajectory was achieved by first creating control-surfaces in CAD whose contours matched the reference curves. In the printing setup, these surfaces were then filled with a concentric multi-ring filler that followed the curvilinear contour (Fig. 1(b)). The axial distance between the reference contours is the shift distance d_s. A similar solution was reported in [32] for the design of optimised composite components.

This procedure creates gaps in the central area of the control-surface and in the corner regions of the rings (Fig. 1(b)), which cannot be filled with cCF/PA material. These areas were filled with Onyx™. Fibre cuts (with a misaligned segment corresponding to the initial printing point) and fibre turnings also occurred in the corner regions of the rings (Figs. 1(b) and 1(c)). In addition, the orientation of the inner rings or beads did not coincide with the orientation of the reference curve defined by Eq. (1): the further the bead is from the reference curve, the greater the deviation of the fibre orientation. This deviation is more accentuated for a large shift distance (d_s in Fig. 1(b)), where the number of equidistant rings or beads is greater.

The contours of the reference surface in this study were sufficiently separated to introduce two cCF/PA rings at the ends of the control-surface (see detail in Fig. 1(b)). This achieved an acceptable amount of reinforcement cCF/PA material, without excessive deviation of the fibre orientation from the reference path. The width of the control-surface at these ends was $w_1 = 4w_b + w_g$, where w_b is the width of the bead and w_g is the minimum gap between the beads in the corner regions, with both dimensions being 0.9 mm. As shown in Fig. 1(b), the shift distance was $d_s = w_1 / \sin(T_1)$. Therefore, the smaller the angle T_1, the greater the distance between the reference contours. To ensure a fibre orientation close to the reference path, a minimum angle of 10° was set for both T_0 and T_1.

The printing of a complete layer was carried out by shifting the control-surface as many times as necessary along the x-axis, as illustrated in Fig. 1(c). This produced a course of beads between the gap zones similar to those created in AFP technology with the tow-drop method [8]. The same procedure was repeated for each layer to produce a laminate. The manufacture and preparation of the specimens is described in Section 4.1.

Using this manufacturing strategy, up to 80% of the surface of the layer was filled with cCF/PA material. In this way, up to 25% of fibre volume fraction was obtained, while for a unidirectional fully filled cCF/PA layer this fraction reached around 31.4%. The sample presented in Fig. 1(c) is a $\langle 45|10\rangle$ configuration ply printed on a white PA layer.

3. Design of open-hole tensile specimens

3.1. Problem statement and design procedure

In this study, a VS laminate for an OHT case was designed, manufactured, and tested, and compared to the QI reference laminate for different hole sizes. This new solution was achieved without increasing the laminate weight, as the same thickness and number of plies were used in both laminates, and the densities of cCF/PA and Onyx™ are equal [26].

The OHT loading direction was the x-axis, and the fibre orientation $\theta(y)$ was defined with respect to this axis, as shown in Fig. 1(a). Specimen dimensions were established following the ASTM D5766 standard recommendations for OHT tests [33]. The width W of the specimen was 36 mm, with a symmetrical and balanced laminate of 16 layers, resulting in a nominal sample thickness of 2 mm. The hole diameter of the reference sample configuration was ∅6 mm, but configurations with ∅3 mm (half the reference) and ∅12 mm (double the reference) holes were also analysed, giving a specimen width-to-hole diameter ratio of 6, 12, and 3, respectively.

The characteristics of the two types of laminates studied are set out in Table 2. The QI laminate followed the standard structure, with ply orientations of 0°, ±45°, and 90°, and a ply ratio percentage of 25/50/25, respectively. The designed VS laminate combined 50% of steered-fibre $\pm\langle T_0|T_1\rangle$ layers with 25% standard straight-fibre layers oriented at ±45°, and 25% at 90°. Straight-fibre layers were included to minimise the effect of manufacturing defects in the steered-fibre layers and to stiffen the weaker directions, thus achieving a robust design. This laminate configuration was the result of a preliminary analysis carried out with the parametric FE model described in the following paragraph. It should be noted that the VS laminate did not contain plies with fibres oriented in the loading direction (0° plies), as a behaviour different to that of traditional laminates was desired. Variable-stiffness laminates with the layup characteristics in Table 2 are hereinafter referred to as VS$\langle T_0|T_1\rangle$.

With this approach, the design variables of the VS laminate were reduced to the orientation of the fibres at the centre T_0 and free edge T_1 of the steered-fibre plies. These orientations were determined by parametric studies in the range of potential $\langle T_0|T_1\rangle$ angles following the procedure applied by Lopes et al. for VS panels [1] and using the commercial finite element (FE) package Abaqus [34]. This parametric model estimated the OHT loads at which damage initiation and ultimate failure occur for each laminate configuration. For this purpose, stress-based failure models were implemented in a Fortran subroutine "UVARM" to obtain the User defined VARiables at FE Material points. The in-plane stiffness (linear and shear) was also determined for each laminate configuration.

In this design-oriented parametric model, no distinction was made between the cCF/PA reinforcement and Onyx™ filler zones of the steered-fibre layers, and homogenised properties were used. These homogenised properties were considered to vary in the layer with respect to the transverse y-position, as the average amount of fibre changes due to the ratio between the reinforcement material and the unreinforced gap. To do so, a model that determines the fibre volume

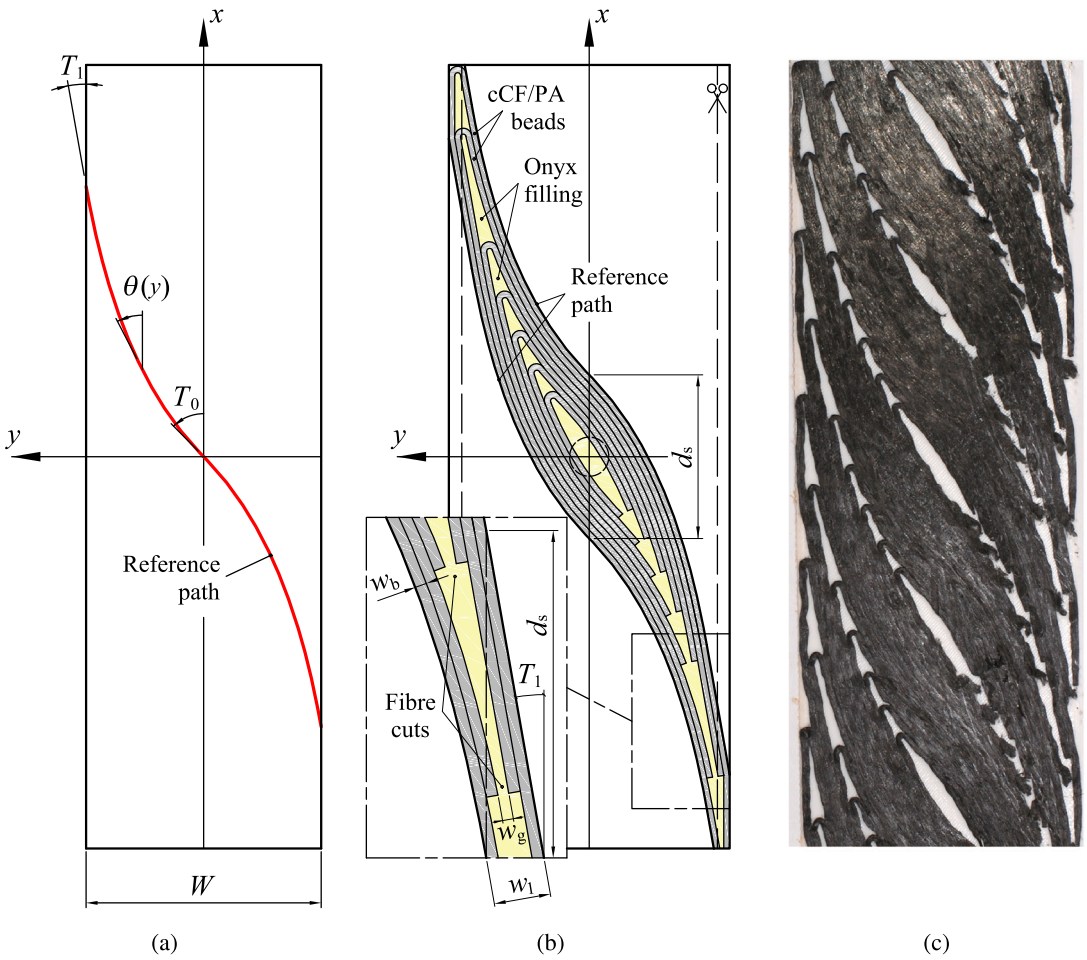

Fig. 1. 3D printing of steered-fibre ply: (a) $\langle T_0|T_1\rangle$ reference fibre path, (b) concentric filling of the control-surface between two reference fibre paths, and (c) $\langle 45|10\rangle$ configuration obtained by shifting the control-surface. This ply was printed on a white PA layer and without Onyx™ filling for better visualisation of the cCF/PA reinforcement.

fraction and the homogenised material properties at each position of the steered-fibre ply was developed. The process of determining material homogenised properties, the failure criteria, and the FE model are described in the following sections. This parametric study configuration was implemented in a user-developed Python script for Abaqus.

3.2. Homogenisation of mechanical properties

The homogenised properties of the steered-fibre plies vary as a function of the transverse y-position, due to the variation of the average fibre quantity. The model developed to estimate fibre content for each position is illustrated in Fig. 2. The unreinforced central gap of the control-surface was assumed to be of constant width and follows the trajectory of the reference curve. The value of this width is $w_b + w_g$ and matches the average width of the gap (Fig. 1(b)). The shift distance between the reference contours is $d_s = (4w_b + w_g)/\sin T_1$, as seen in Section 2.2, from which the distance $d_g(y) = (w_b + w_g)/\sin\theta(y)$ contains no reinforcement (Fig. 2). Thus, the fibre volume fraction is determined by the following ratio:

$$v_f(y) = v_f^{raw}\frac{d_s - d_g(y)}{d_s} \tag{2}$$

where $v_f^{raw} = 33.9\%$ is the fibre volume fraction of the raw material of the filament [27]. The equation shows that the smaller the angle θ, the smaller the amount of fibre. This can also be seen in Fig. 1(b), where the quantity of beads and fibre is less at the free edge, an area with a lower θ fibre orientation.

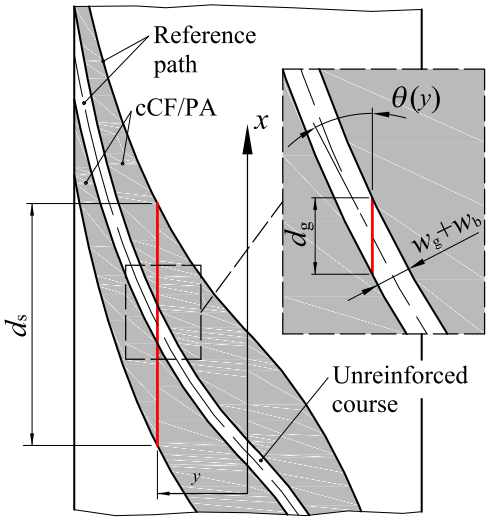

Fig. 2. Model developed to estimate the average fibre content at a transverse y-position.

The homogenised elastic properties at each position of the steered-fibre ply were determined with the methodology proposed by Polyzos et al. [35], in two steps. Firstly, the properties of the raw material composed of carbon fibre and PA matrix are determined by means of

Table 3
Effective properties of the constituents obtained from reverse engineering of the in-plane ply properties.

Carbon fibre elastic properties	E^{f}_{11} = 215 GPa; E^{f}_{22} = 8.0 GPa; ν^{f}_{12} = 0.32; G^{f}_{12} = 20.0 GPa; G^{f}_{23} = 18.0 GPa
Carbon fibre strength	X^{f}_{T} = 2900 MPa; X^{f}_{C} = 1400 MPa
Polyamide matrix elastic properties	E^{m} = 3.1 GPa; ν^{m} = 0.48

the micro-mechanical model of Chamis [36]. Then, the properties of the characteristic meso-structure created in the 3D printing process are estimated using the void-model of Rodríguez et al. [37]. This second step takes into account the voids that are created mainly between the cCF/PA beads during printing, which significantly reduce the material properties. This procedure is detailed in Appendix.

The fibre and matrix effective properties required to apply the homogenisation model were predicted using reverse engineering from the experimental in-plane ply properties (shown in Table 1 and reported in [13]) and using the micro-mechanics and void-model equations (Eqs. (A.1)–(A.3)). A similar procedure was carried out by Chamis et al. [38] using optimisation subroutines, in a multi-scale methodology. These effective properties take into account any degradation or improvement in the bulk constituent material properties caused by thermal residual stresses from the printing process, environmental effects, and/or the fibre-matrix interface. The predicted effective properties, shown in Table 3, were consistent with the provided fibre and matrix material properties [27,39,40]. The in-plane ply properties obtained from these values showed good agreement with the experimental results. The error was less than 1%, except for the Poisson's ratio, which is underestimated by the model, with an error of 4%. This result was also observed by Rodríguez et al. [37] and could be due to molecular orientation effects in the matrix of the extruded beads.

3.3. Failure criteria

At present, there is little published data on the failure mechanisms and criteria for 3D printed continuous fibre composites. However, the printed cCF/PA material exhibits a mechanical behaviour similar to that of traditional orthotropic unidirectional composites [13], which have been the subject of much study in recent decades. It is therefore possible to adapt or extend existing criteria to the behaviour of printed composites, as has been done in preliminary studies [41–43]. Based on this idea, the failure criteria developed for traditional composite materials were used and adapted in this study, as described in the following sections.

3.3.1. First-ply failure criteria

The onset of damage or the first-ply failure (FPF) was determined by the LaRC failure criteria. These stress-based criteria analyse the physics associated with the failure process at the micro-mechanical level and apply it at ply and laminate level. It is determined from the stress distribution of each layer, obtained by the FE method in this study, and from the in-situ strengths of the plies. The latest development of LaRC criteria is LaRC05 by Pinho et al. [44,45], which distinguishes between matrix cracking, fibre kinking and splitting, and fibre tensile failure. The failure indexes (FI) corresponding to these three failure modes are determined according to Eqs. (3). Failure occurs when the index reaches a value of 1.

$$\mathrm{FI_M} = \left(\frac{\tau_T}{S^{is}_T - \eta_T \sigma_N}\right)^2 + \left(\frac{\tau_L}{S^{is}_L - \eta_L \sigma_N}\right)^2 + \left(\frac{\langle \sigma_N \rangle_+}{Y^{is}_T}\right)^2 \tag{3a}$$

$$\mathrm{FI_{Kink/Split}} = \left(\frac{\tau^{m}_{23}}{S^{is}_T - \eta_T \sigma^{m}_2}\right)^2 + \left(\frac{\tau^{m}_{12}}{S^{is}_L - \eta_L \sigma^{m}_2}\right)^2 + \left(\frac{\langle \sigma^{m}_2 \rangle_+}{Y^{is}_T}\right)^2 \tag{3b}$$

$$\mathrm{FI_{FT}} = \frac{\langle \sigma_1 \rangle_+}{X_T} \tag{3c}$$

The matrix failure criterion (Eq. (3a)) is an adaptation of the Mohr–Coulomb failure criterion for unidirectional composite plies. τ_T, τ_L and σ_N are transverse shear stress, longitudinal shear stress, and normal stress in the fracture plane, respectively, and are obtained by stress transformation [44]. The strengths Y^{is}_T, S^{is}_L and S^{is}_T are the in-situ transverse tensile strength, longitudinal shear strength, and transverse shear strengths, respectively, and account for the increase in strength due to the constraining effect of adjacent layers. The friction or slope coefficients η_L and η_T represent the effect of pressure on the failure response. The third term of the criterion represents the contribution of normal traction to crack opening.

Table 4
In-situ strengths (MPa) of the printed cCF/PA composite for each ply configuration.

Ply configuration	Y^{is}_T	S^{is}_L	S^{is}_T
Thin embedded ply	47.9	60.8	40.0
Thin outer ply/Embedded clustered plies	39.8	55.2	36.9

In this study, a transverse slope coefficient η_T of 0.29 was considered, obtained from the pure transverse compression test and assuming a fracture angle of 53°, which is typical for laminated composites. The longitudinal slope coefficient η_L is calculated from biaxial failure envelopes. This characterisation is not yet available for the printed material, so a value of 0.1 was assumed, based on the recommendations for carbon fibre reinforced composites [45]. Fracture mechanic models of crack propagation in constrained layers were used to calculate these in-situ strengths [44,46,47]. The initial energy release rate was considered for crack growth, and transverse and shear behaviours were assumed to be non-linear, using the mechanical characterisation previously performed and reported in [13,28,48]. The in-situ strength values calculated for the different ply configurations are presented in Table 4.

The fibre kinking or splitting criterion is given in Eq. (3b). σ^{m}_2, τ^{m}_{12}, and τ^{m}_{23} are the stresses in the misalignment frame, and are obtained by stress transformation [44]. The fibre misalignment angle depends on the initial misalignment angle (manufacturing defect) and the shear strain produced by the stress state. An initial misalignment angle of 4.5° was estimated from the longitudinal compression test results reported in [13] and set out in Table 1. This initial misalignment is higher than that of traditional composites, indicating that the printed material inherently contains more manufacturing defects (fibre misalignment and waviness, voids, etc.), which favours fibre kinking and reduces compressive strength. This behaviour was also noted by Tang et al. [43] and Zhang et al. [31].

The last criterion is the fibre tensile failure criterion, which is based on the maximum stress criterion, as stated in Eq. (3c). X_T is the longitudinal tensile strength, reported in [13] and shown in Table 1 for straight-fibre plies and determined by Eq. (A.3) for the steered-fibre plies.

3.3.2. Ultimate failure criteria

Multidirectional laminates can accumulate damage and redistribute load after the onset of damage, withstanding a considerable increase in load before ultimate failure (UF) [49]. The failure mechanism of composites is complex, but a number of failure models have been developed to predict the notch strength of a laminate [50]. These include simplified models such as the stress-based, which provide a reasonably accurate notched strength prediction with simple computations and a relatively low amount of mechanical tests. This makes them suitable for preliminary designs based on parametric studies, as in the present study.

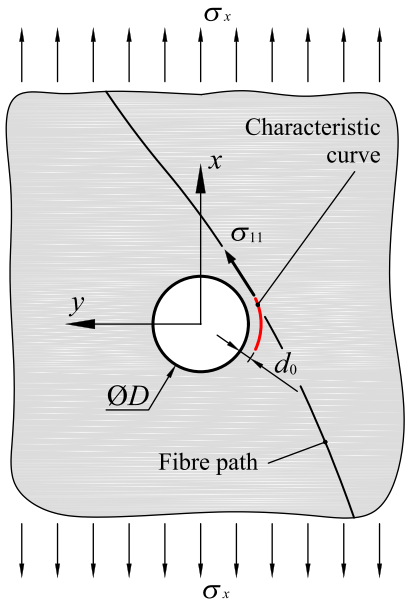

Fig. 3. Application of the ultimate failure PSC model in the steered-fibre ply.

One of the first and most widely used stress-based models developed for the prediction of the notched strength of fibre-dominated laminates is that proposed by Whitney and Nuismer [51] and extended by Chen et al. [52]. In this model, ultimate failure occurs when the elastic stress in the load-bearing ply at a distance from the edge of the hole (point stress criterion (PSC)), or the average stress over a distance (average stress criterion) reaches the ultimate longitudinal strength of the un-notched unidirectional laminate. This dimension is known as the characteristic distance d_0, and represents the distance below which the material must be critically stressed to produce the ultimate failure of the laminate.

In this study, the PSC model was applied to the load-bearing ply, but with some modifications due to the laminate characteristics. The load-bearing plies considered were the 0° ply for the QI laminate and the steered-fibre ply for the VS laminate. In the latter, the maximum longitudinal stress S_{11}, which in traditional laminates is on the transverse axis through the hole (y-axis in Fig. 3), is slightly displaced due to the oblique fibre orientation. Therefore, a circular characteristic curve of radius $D/2 + d_0$ was defined (Fig. 3), where the failure criterion given in Eq. (4) was applied. Thus, the ultimate failure of the laminate results when the longitudinal stress S_{11} reaches the tensile strength X_T of the ply at any point on the characteristic curve. In the case of the QI laminate, the point of analysis is at the intersection of the characteristic curve with the y-axis (Fig. 3). The longitudinal tensile strength X_T of the 0° layer of the QI laminate is obtained from the mechanical characterisation of the material (Table 1), and that of the VS layer is obtained from the homogenisation process (Eq. (A.3)).

$$\mathrm{FI_F} = \frac{\sigma_{11}|_{r=(\frac{D}{2}+d_0)}}{X_T} = 1 \tag{4}$$

The characteristic distance d_0 was considered as a laminate property independent of the hole size, based on the results reported by Chen et al. [52] for fibre-dominated well dispersed laminates. The characteristic distances were determined by performing OHT tests on reference laminates for a ∅6 mm hole diameter.

3.4. Finite element method implementation

The VS laminate for the OHT case was designed with a parametric study using the commercial FE package ABAQUS [34]. For this purpose, several FE models based on incremental displacement static analysis were developed to calculate the OHT strength and stiffness of the laminates.

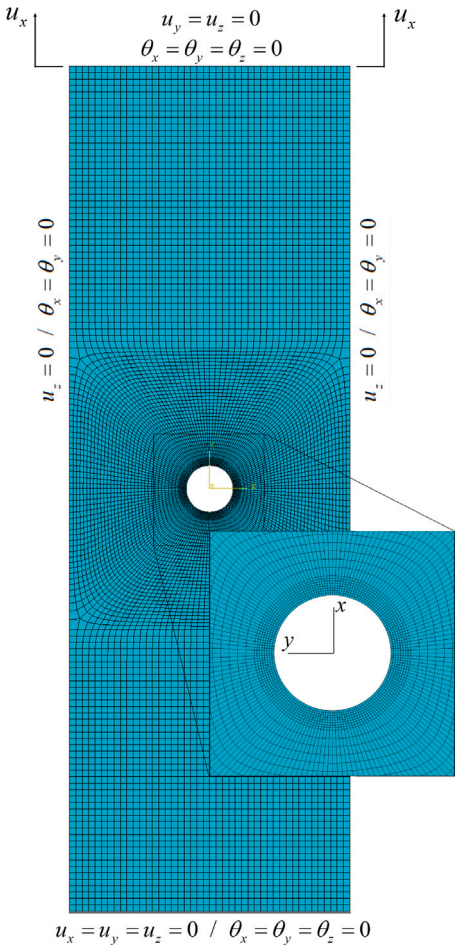

Fig. 4. Boundary conditions and meshing of the FE model for the calculation of the OHT strength. A finer mesh was applied to the hole contour for accurate prediction.

The boundary conditions of the OHT test (Fig. 4) were modelled as follows:

- On the lower edge, the embedded condition was modelled by constraining all degrees of freedom.
- On the top edge, a positive longitudinal displacement in direction x was imposed, and all the other degrees of freedom were constrained.
- On the lateral free edges, the out-of-plane degrees of freedom were constrained.

The length of the specimen in the model was three times its width, which was long enough to ensure that the boundary conditions did not alter the behaviour of the critical zone.

The failure criteria (FPF and UF) described in the preceding section were implemented in a special purpose Fortran subroutine UVARM. This subroutine post-processes the stress components for the calculation of the LaR05 criteria failure indices, and was run at each displacement increment and for each integration point of the FE model. A gradual and refined displacement increment ensured an accurate capture of the load level at which the FPF and UF criteria were met. The load level was determined by the axial reaction force produced in the clamped of the specimen, from which the OHT strength was calculated using the gross cross-sectional area (disregarding the hole).

For efficiency reasons, the analyses carried out in this work were based on shell models. Thus, it was considered that failure was mainly driven by the in-plane components of the stress tensor and dominated by the fibre behaviour with little subcritical damage and delamination. Reduced integration quadrilateral shell elements (S4R) were used in the model, with a general edge length of 1/44 of the specimen W width. For the VS laminates, each element of the FE model was associated with a specific lay-up with homogenised material properties. Both the fibre orientation and homogenised properties were determined based on the centroid position of each element and using the equations presented in Sections 2.2 and 3.2. Therefore, the variation in fibre orientation can be considered to be discrete in the model. Between two neighbouring elements, the maximum difference in fibre angle was 3.6°.

A higher mesh density, with elements of around 0.13 mm edge length, was used in the hole contour (Fig. 4). This provided sufficient resolution to distinguish the strength of different laminates when applying the PSC criterion to the characteristic curve. In FPF analysis, the mesh size influences the damage prediction at the hole edge, and thus the calculation of the laminate strength, i.e. the smaller the element size, the lower the strength value. Green et al. [49] observed that in notched QI laminates sub-critical damage starts in off-axis layers with matrix cracking and splitting, accompanied by local delamination areas that are similar in size to the thickness of the ply. For this reason, at the edge of the hole a mesh size similar to the layer thickness was used in this study (Fig. 4).

To determine the in-plane stiffness (E_x, E_y and G_{xy}) of the different laminate configurations, three FE models were developed from the strength model described above. In these models, a specimen length of 36 mm (equal to its width) was assumed. The specimen model was meshed using shell elements, with a general edge length of a 1/44 of the specimen width W. In this case, the mesh was not refined around the hole contour, as it has little influence on the overall stiffness of the specimen. The boundary conditions applied for the linear stiffness determination were the same as those applied in the FE strength model (Fig. 4), but with complementary fibre orientations in the transverse stiffness case. On the other hand, to determine the shear stiffness G_{xy}, a transverse displacement was imposed on the upper edge (y-axis), keeping the lower edge constrained.

The FE calculations of the parametric model were performed discretely for each 1° at T_0 in the 10° − 90° range and for each 5° at T_1 in the 10° − 40° range. As explained in Section 2.2, a minimum angle of 10° was set for both T_0 and T_1 to ensure that the fibres steered close to the reference path.

3.5. Design results

The FPF and UF strengths under open-hole tensile loading for different VS⟨$T_0|T_1$⟩ combinations and for the reference ∅6 mm hole case are plotted in Fig. 5. Each curve corresponds to a value of T_1, and the strengths of the reference QI laminate are represented in dashed lines. The highest FPF and UF strength resulted from the smallest T_1 angle of 10°, i.e., with a fibre orientation at the specimen free edges close to the loading direction. Regarding T_0, the maximum strength was achieved for values between 40°−50°. For lower values, i.e., with a fibre orientation close to the loading direction, failure was initiated at the edge of the hole, as in the QI laminate. In contrast, for high values of T_0, failure was initiated at the free edge, out of the hole. The maximum strength occurred at the transition of the fracture from one zone to the other, providing a significant improvement over the QI laminate. In addition, many of the VS⟨$T_0|T_1$⟩ combinations were more resistant than the QI laminate (Fig. 5).

The reason for the superior performance of VS laminate compared to straight-fibre QI laminate, is a favourable load distribution across the width (y-coordinate) of the specimen, as shown in the fibre failure index fields in Fig. 6. For the QI laminate (Fig. 6(a)), the location of the most stressed area is clearly limited to the apex of the hole, due to the stress concentration effect. In the VS laminate, the configurations for which the OHT strength is high present medium values of the fibre orientation angle at the centreline and low values at the free edges of the specimen. This is similar to the configuration illustrated in Fig. 1(c). The local axial stiffness is high in the areas of the laminate where the fibres are aligned with the loading direction. This results in most of the load being carried by the high stiffness regions of the laminate near the free edges of the specimen (Fig. 6(b)) and the central section only carrying a small fraction of the load, making it very resistant to OHT loading. In addition, a larger portion of the VS laminate contributes to the load-bearing capacity of the specimen, as the value of the critical failure index is more evenly distributed in the specimen (Fig. 6(b)).

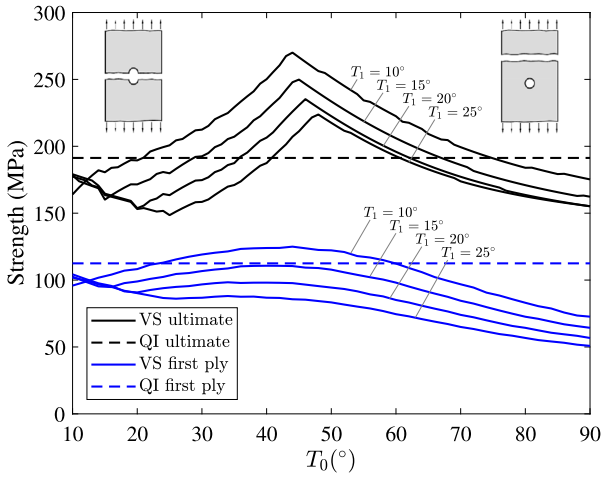

Fig. 5. FPF and UF strength curves of the VS laminate for the ∅6 mm hole reference case. At T_0 values below the maximum strength, fracture occurs through-hole, while at higher values it occurs out-of-hole.

The onset of damage or first ply failure, for both QI and VS laminates, was caused by matrix tensile failure in the 90° layers at the hole apex. This took place for the QI laminate at approximately 60% of the ultimate load. Additionally, the FPF strength of the VS laminate was higher than the QI laminate for medium T_0 and low T_1 values (Fig. 5). This may be due to the redistribution of the load, i.e., for this configuration the central area of the VS laminate is unloaded and therefore the material in this area is less stressed.

The in-plane stiffness of the VS laminate versus QI laminate for the optimum edge fibre orientation T_1 of 10° is shown in Fig. 7. The linear stiffness of the VS laminate was lower than the stiffness of the QI laminate, except for low and high T_0 values, where the fibre is aligned with the x and y axes respectively. This decrease in stiffness is due to the lower amount of fibre in the steered-fibre plies compared to the straight-fibre plies. In addition, the QI laminate contains 0° plies, which provide the highest axial stiffness. In general, the higher the central fibre orientation angle T_0, the lower the axial stiffness E_x and the higher the transverse stiffness E_y. It can thus be concluded that the most balanced VS laminate is VS⟨42|10⟩ which shows similar axial and transverse stiffness, and a higher shear stiffness than the QI laminate. For this optimal configuration, the ultimate OHT strength was 36.2% higher than that of the QI laminate, and the linear stiffness was 13.2% lower.

The OHT behaviour of the VS laminate for different hole sizes is shown in Fig. 8, for the optimum fibre orientation T_1 of 10° at the free edge. It can be observed that the larger the hole size the more fibre inclination at centreline T_0 is required. This results in more fibre bending to overcome the geometrical discontinuity and transfer the load from the central zone to the outer stiff band, away from the hole. Moreover, for angles T_0 greater than 55°, the failure is initiated at the outer free edges for the different hole sizes, and the strength of the VS laminate is barely affected by the presence of a central hole (Fig. 8).

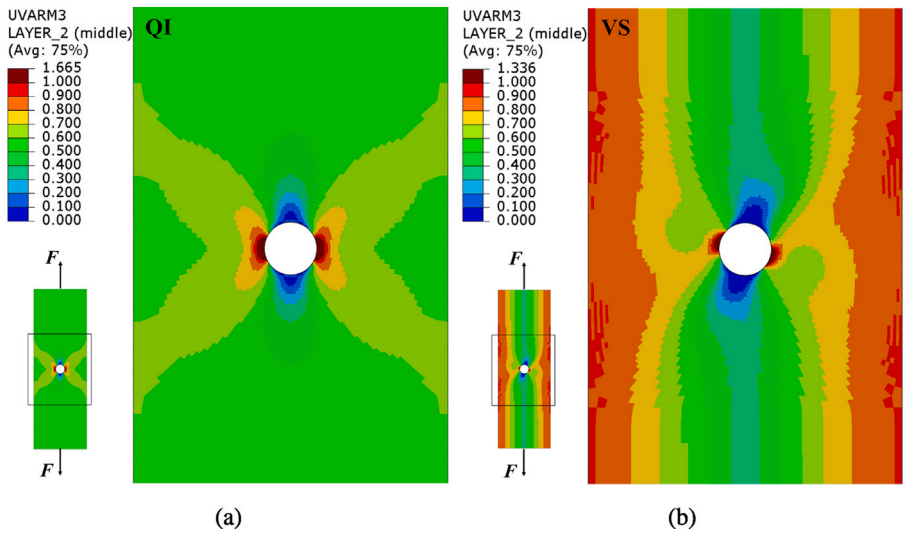

Fig. 6. Fibre tensile failure index field in the load-bearing ply for ∅6 mm hole case at ultimate failure state: (a) 0° ply of the QI laminate, and (b) steered-fibre ply of the VS⟨42|10⟩ laminate.

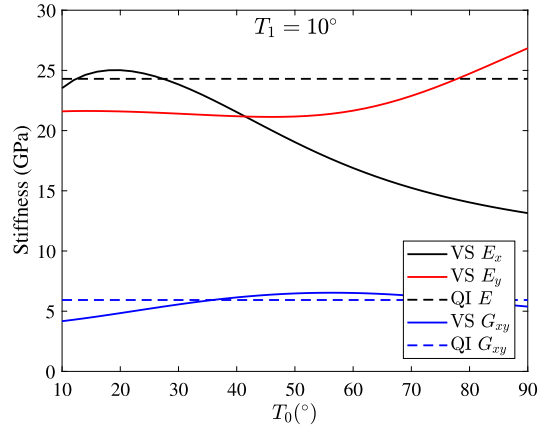

Fig. 7. In-plane stiffness behaviour of the VS laminate for the ∅6 mm hole reference case and for an optimal edge fibre orientation T_1 of 10°.

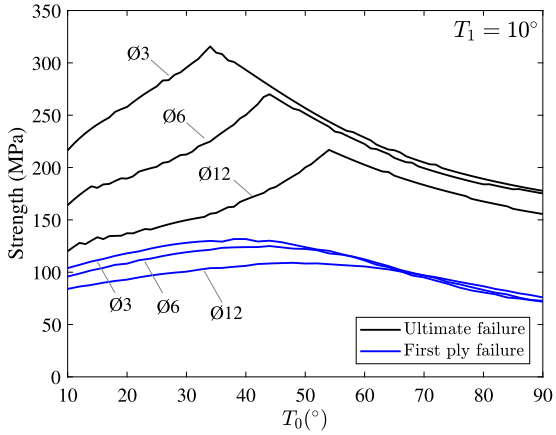

Fig. 8. OHT Strength behaviour of VS laminates for different hole sizes for an optimal edge fibre orientation T_1 of 10°. Diameter values are in mm.

The ultimate strength values were determined by the PSC, which requires knowledge of the characteristic distance d_0, as described in Section 3.3.2. This model calibration was carried out for each type of laminate by performing OHT tests on reference configurations. In the QI laminate, the calibration was performed for a ∅6 mm hole, and the characteristic distance obtained was 0.95 mm. In the VS laminate, the calibration was performed for a VS⟨40|10⟩ combination and ∅6 mm hole, and the characteristic distance obtained was 0.7 mm. This difference between the laminates may be due to the configuration of the laminate itself and the fact that homogeneous properties are used in the case of the VS laminate. These characteristic distance values were used to predict the strength of all other hole sizes and $\langle T_0|T_1\rangle$ combinations in the case of the VS laminate. The experimental procedure for the OHT tests is described in Section 4.1.

4. Experimental validation

4.1. Test plan and methods

The laminate type and hole size of the OHT tests conducted are set out in the first three columns of Table 5. Tests were carried out for three hole sizes (∅3, ∅6 and ∅12 mm), while the QI laminate was also tested in the un-notched condition. The VS laminates were tested in the optimal configurations determined by the results of the FE parametric study presented in Section 3.5. Various combinations of hole sizes T_0 angle increments of 5° were tested: VS⟨35|10⟩ for ∅3 mm, VS⟨50|10⟩ for ∅12 mm and for the ∅6 mm hole case two configurations (VS⟨40|10⟩ and VS⟨45|10⟩). The latter were carried out to observe the change of the fracture zone from the through-hole to out-of-hole.

The specimen dimensions and test methodology were established following the ASTM D5766 standard recommendations [33]. The length of the specimens was 250 mm, with a nominal width and thickness of 36 mm and 2 mm, respectively, as described in Section 3.1.

The stacking sequences of the 16 composite layers of the QI and VS laminates are shown in Table 2. The aim was to minimise the difference in fibre orientation of adjacent layers to reduce delamination and matrix cracking. A single Onyx™ layer of both floor and roof was used to manufacture the specimens, resulting in an 18-layer laminate. These two outer layers were not taken into account in the nominal cross-section in both the model and the experimental data processing. To ensure sufficient compaction of the printed bead, and thus adequate adhesion between the layers, special care was taken in levelling the bed and adjusting the height of the nozzles. For this purpose, the test prints available in the printer were used, as recommended by the manufacturer. This also minimises fibre waviness during the printing process. Despite the adjustment, the average thickness of the printed samples was 2.10 ± 0.05 mm, 4.8% thicker than nominal.

Table 5
Mechanical properties of the tested QI and VS laminates. The OHT strength and E_x modulus determined with the homogenised model are included. The energy absorption per unit volume up to fracture is calculated as the area under the stress–strain curve.

D (mm)	W/D	Laminate	OHT strength (MPa)		E_x modulus (GPa)		Ultimate strain (%)	Energy absorp. (kJ/m^3)
			Test	Model	Test	Model	Test	Test
Un-notched	–	QI	382.6 ± 9.3	–	26.2 ± 0.4	–	1.45 ± 0.03	2756 ± 122
∅3	12	QI	244.7 ± 7.2	252.5	25.3 ± 0.1	25.7	0.97 ± 0.03	1197 ± 78
∅3	12	VS⟨35|10⟩	269.1 ± 8.4	309.8	22.8 ± 0.4	23.6	1.20 ± 0.02	1636 ± 78
∅6	6	QI	193.0 ± 1.8	191.3	25.2 ± 1.0	25.2	0.79 ± 0.05	779 ± 69
∅6	6	VS⟨40|10⟩	249.1 ± 4.7	250.2	21.2 ± 0.6	21.9	1.22 ± 0.02	1557 ± 53
∅6	6	VS⟨45|10⟩	250.1 ± 4.1	266.5	19.9 ± 0.4	20.6	1.31 ± 0.04	1683 ± 62
∅12	3	QI	144.0 ± 0.2	138.5	22.7 ± 0.2	22.9	0.65 ± 0.01	484 ± 18
∅12	3	VS⟨50|10⟩	188.8 ± 5.8	200.1	17.8 ± 0.1	18.5	1.10 ± 0.04	1068 ± 79

The specimens were printed one by one. The concentric filling of the control-surface created contours on the free edge whose orientation did not match the reference path (see Fig. 1(b) in Section 2.2). Therefore, the specimens were printed with an over-width, that was later removed to the nominal width W with an automatic grinder with 240 grit SiC paper. The average width of the samples was 35.95 ± 0.06 mm.

The holes were milled with finishing end mill tools at a feed rate of 100 mm/min and a cutting speed of 56 m/min. The samples were clamped between two steel templates to prevent delamination or other damage to the material surrounding the hole. The relative position of the hole with respect to the reference path in the steered-fibre layers is depicted in Fig. 1(b). The hole was located in the centre of the control-surface and no ply staggering was applied between the successive layers in this study. The hole was not directly printed because it is not possible to produce the desired trajectories in the hole area with the filling strategies available in the Mark Two™ printer (described in Section 2). This approach would include continuous fibre in the hole contour (local reinforcement), which is outside the scope of this study, more focused on the global performance of the laminate.

Tabs were used on the un-notched and ∅3 mm QI laminate specimens and all VS laminate specimens, ensuring proper load transfer and specimen fracture in the calibrated area. Since PA is a hygroscopic polymer, all the specimens were conditioned prior to testing. Three repetitions of each laminate configuration were tested.

OHT quasi-static tests were performed on a universal testing machine (Zwick/Roell) equipped with a 50 kN load cell and at a load-rate of 2 mm/min. The longitudinal strain of the specimens was measured with a Zwick/Roell extensometer at a calibrated length of 80 mm, while the strain state was analysed by a Gom-Aramis digital image correlation system (DIC). The measuring area of the DIC system was 100 × 85 mm^2 with a resolution of 5 Mpx. The subset pixel size was 19 × 19 with a 15 pixel step size, and the frame rate was 3 fps.

4.2. Test results

The stress–strain curves resulting from the OHT test are plotted in Fig. 9, and the corresponding fracture and DIC strain field images of the QI and VS laminates are shown in Figs. 10 and 11, respectively. The measured mechanical properties are compiled in Table 5.

The QI laminate presented a highly linear and brittle behaviour for all the cases studied (Figs. 9(a) and 10(b)). The fracture plane was transverse to the loading direction (Fig. 10(b)), and in the OH cases fracture initiated at the hole apex and propagated towards the free edges. In the un-notched case, several fracture planes were observed, which could be caused by the high energy released when the laminate broke. The strain field measured by DIC shown in Fig. 10(a) reveals a considerable increase in strain at the apex of the hole before fracture. This may be due to damage occurring at the notch, which redistributes the stress concentration and delays the occurrence of breakage. The main failure mechanism was fibre breakage. However, matrix shear cracking in the 45° layers and delamination between the 45° and 0° layers were also observed.

The behaviour of the VS laminates was also linear and brittle, as shown in Figs. 9 and 11(b). The fracture plane was transverse to the loading direction, but some configurations fractured outside the hole, such as VS⟨35|10⟩ for ∅3 mm and VS⟨45|10⟩ for ∅6 mm. The transition from through-hole to out-of-hole breakage predicted by the model was observed in laminates VS⟨40|10⟩ and VS⟨45|10⟩ for a ∅6 mm hole. In the DIC images just before the fracture, maximum levels of axial deformation ϵ_x were found at the hole apexes and in localised areas near the free edge (Fig. 11(a)). These latter coincide with the failure initiation area of out-of-hole fracture cases (Fig. 11(b)). As in the QI laminates, the failure mechanism was fibre-dominated, but triangular-shaped delaminations near the free edge accompanied by matrix cracking were observed in the VS laminates (Fig. 11(b)).

5. Discussion

The effect of hole size on the two types of laminates analysed, from the results of the test and the model, is shown in Fig. 12.

The behaviour of the QI laminate follows the characteristic trend, with a significant reduction in strength due to the notch effect. In the ∅6 mm hole reference laminate, the strength decreased by 49.6% compared to the un-notched laminate. The model predicted the notched laminate behaviour with good accuracy (Table 5 and Fig. 12): the maximum deviation of the model from the test results was 0.9% for the stiffness and 3.8% for the strength (for ∅12 mm hole size). This confirms that the PS criterion with a fixed characteristic distance is suitable to estimate the notched strength of printed cCF/PA fibre-dominated laminates with low sub-critical damage, as also demonstrated in previous works for traditional composites [49,52].

In the VS laminate, on the other hand, the homogenised model accurately estimated the stiffness, but overestimated the laminate strength for the out-of-hole fracture cases (up to 15.1% for the ∅3 mm case, see Table 5). This may be due to the effect of manufacturing constraint-induced defects, such as Onyx-filled gaps and fibre discontinuity (Fig. 1(b)), which were not reproduced in the homogenised model. For further analysis, a FE model including manufacturing defects was developed for the case of VS⟨45|10⟩ with a ∅6 mm hole. As in the parametric model, shell elements were used but with a regular mesh size of 0.25 mm. Based on the centroid position of each element, the material and fibre orientation for the steered-fibre layer was determined: Onyx™ properties for the elements in the gaps and cCF/PA properties (Table 1) for the elements in the reinforced paths. The fibre orientation of these latter elements coincides with the fibre orientation of the reference curve at its nearest point, because the concentric filling in the printing process creates equidistant fibre paths (Fig. 13(a)). Similar as-manufactured modelling was carried out by Falcó et al. [8] for tow-steered laminates.

The results of this as-manufactured model show that fibre tensile fracture is produced in the high stiffness regions near the free edges,

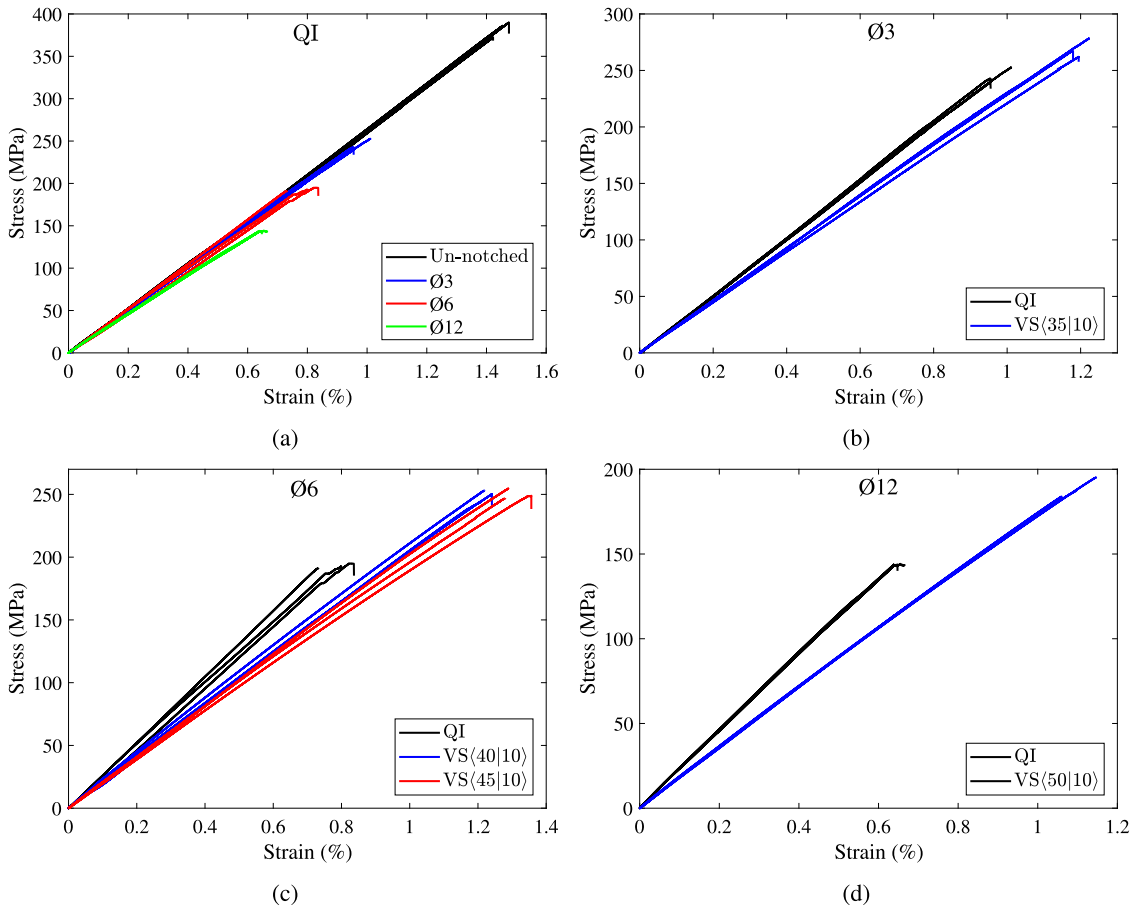

Fig. 9. Stress–strain curves of the OHT tests: (a) QI laminate behaviour for different hole sizes and (b), (c), and (d) QI and VS laminate behaviour for ∅3, ∅6, ∅12 mm hole sizes, respectively. Three repetitions of each laminate configuration were performed.

which is further amplified by the stress concentration effect produced by the gaps (Fig. 13(b)). In the same area, the onset of matrix damage also occurs first in the central 90° straight-fibre layers, and then in the outer 45° straight-fibre layers (Fig. 13(c)). The model predicted that this damage initiated at 47% of the ultimate load, with a load level similar to the damage initiation of the QI laminate at the hole apex. This behaviour was also found in the tests, where it was observed that the fibre-free area is the zone of highest strain and matches the origin of the fracture plane (case ∅6 mm VS⟨45|10⟩ in Fig. 11(a)). Moreover, this geometric discontinuity combined with the edge-effect amplified interlaminar stresses, even producing small delaminations, as shown in the fracture images (Fig. 11(b)). Nevertheless, this combination of straight-fibre and steered-fibre layers can significantly reduce the negative effect of these manufacturing defects.

The homogenised parametric model was calibrated to take into account the stress concentration effect caused by manufacturing defects. For this purpose, a reduced fibre failure index was considered in the outer bands close to the free edges. An average FI value of 0.9 was estimated from the test results of the out-of-hole fracture cases. The results of this calibrated parametric model versus the QI laminate for different hole sizes are shown in Fig. 12. As discussed in Section 3.5, the larger the size of the hole, the greater the inclination of the fibre at the centreline T_0. In this way, the load is transferred from the central area to the outer bands, away from the hole, resulting in a favourable load distribution. For a ∅3 mm hole the ideal laminate configuration is VS⟨31|10⟩ and a 20.5% increase in OH strength over the QI laminate is predicted. For a ∅6 mm hole the ideal laminate is VS⟨41|10⟩ with a 32.4% increase in strength, and for a ∅12 mm hole the optimum laminate is VS⟨52|10⟩ with a 39.4% improvement in strength. Therefore, it can be stated that the VS laminate makes better use of the load-bearing capacity of the material for large holes (small W/D ratios) compared to the QI laminate. For holes below ∅1 mm no improvement is predicted. This may be because the influence of manufacturing defects is greater than that of the hole in this case.

As shown in the results of the VS laminate (Fig. 9 and Table 5), the increase in strength is accompanied by a decrease in stiffness, which is counter-intuitive behaviour. Typically, in conventional laminates, there is a loss in both stiffness and strength, but a gain in ultimate strain. In contrast, in the VS laminates of this study, the maximum strength and strain are increased at the same time. This makes energy absorption (area under the stress–strain curves in Fig. 9) increase dramatically, which can be very positive. For example, the VS⟨40|10⟩ laminate tested for the ∅6 mm hole reference case showed a loss in stiffness of 15.8% and an increase in strength of 29.1% compared to the QI laminate. This resulted in an increase in energy absorption of 99.9% (Table 5). This behaviour can also be seen in the DIC images (Figs. 10(a) and 11(a)), where the strain is more evenly distributed in the VS specimen, indicating that a much larger portion of the laminate contributes to the load carrying capacity of the specimen.

Finally, it is worth noting that the improved performance is achieved with a lower amount of continuous fibre (approximately 10% less than QI laminate). This is due to the gaps created in the printing of the steered-fibre layer, which results in a lower material cost.

6. Concluding remarks

In this study, variable-stiffness 3D printed laminates were designed, manufactured, and tested to improve open-hole tensile behaviour compared to constant-stiffness QI laminates. FFF 3D printing of steered fibre composites has great manufacturing potential, and is ideally

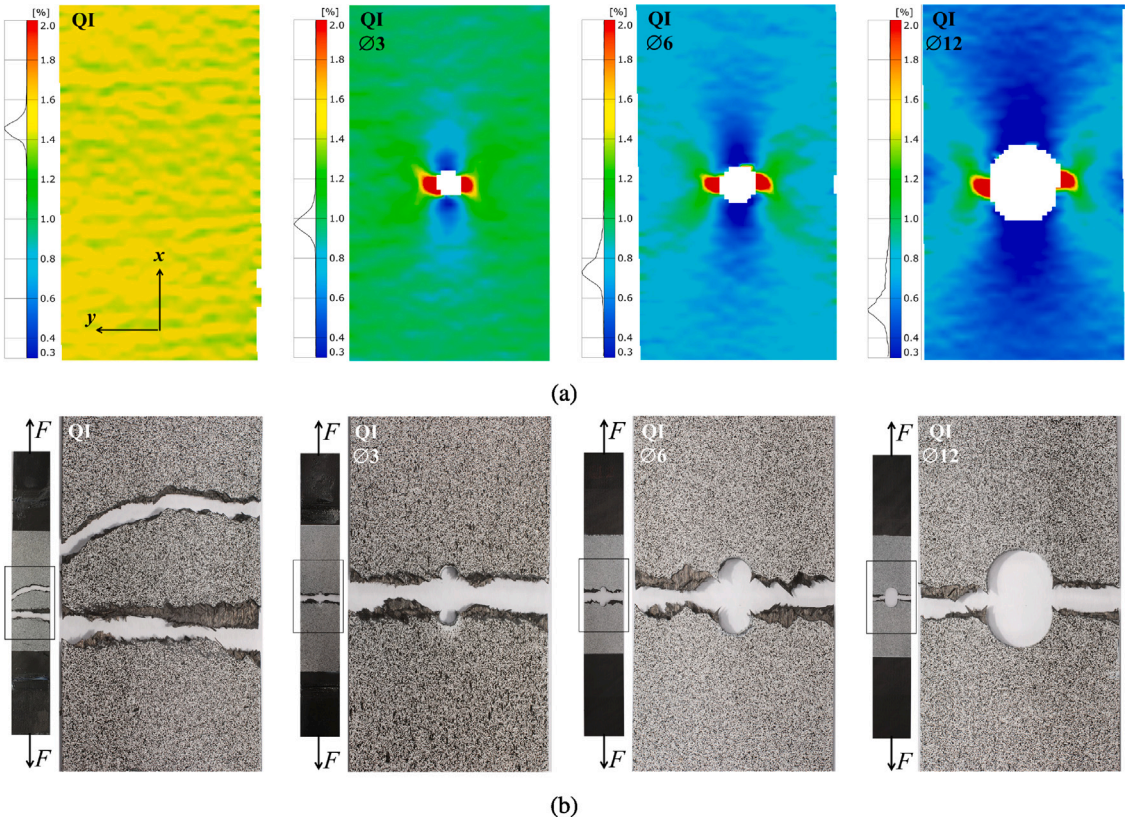

Fig. 10. QI laminate test results for the un-notched case and for various hole sizes: (a) ϵ_x strain field on the outer layer of 45° just before final failure measured by DIC, and (b) fracture images. Diameter values are in mm.

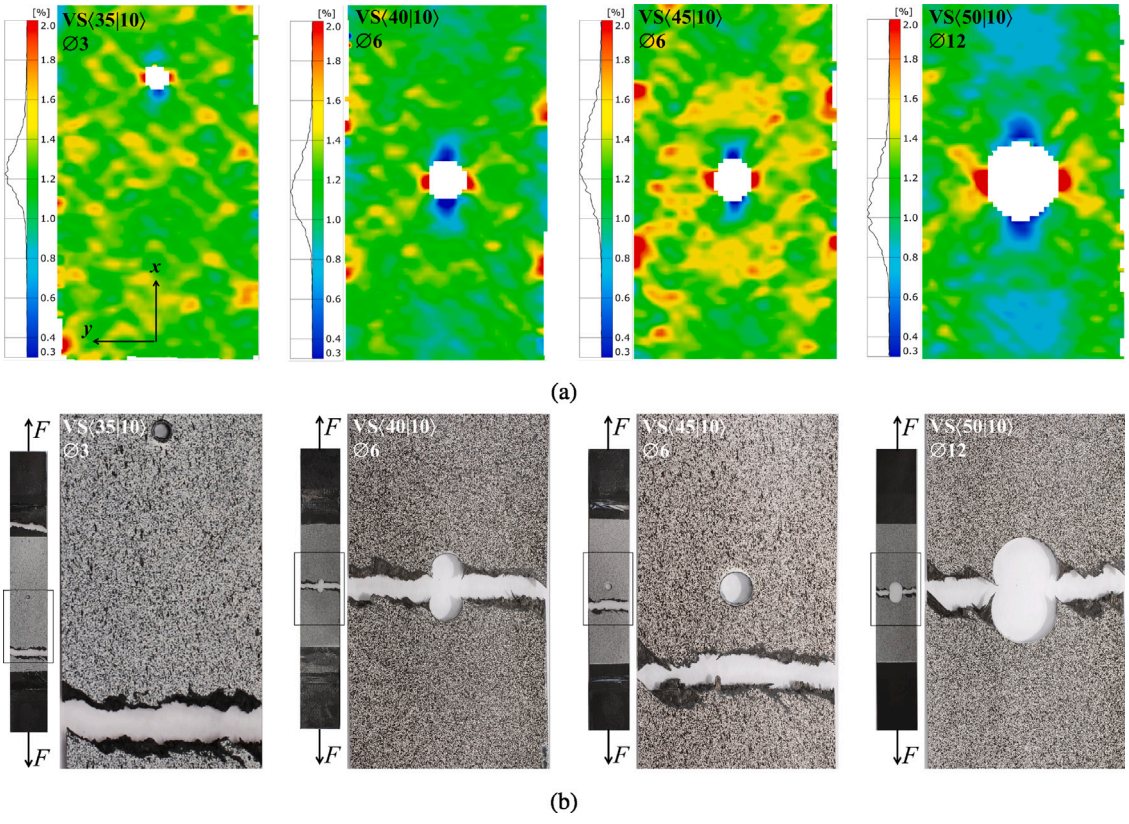

Fig. 11. VS laminates test results for different hole sizes and configurations: (a) ϵ_x strain field on the outer layer of 45° just before final failure measured by DIC, and (b) fracture images. Diameter values are in mm. The configurations VS⟨35|10⟩ for ∅3 mm and VS⟨45|10⟩ for ∅6 mm were fractured out-of-hole.

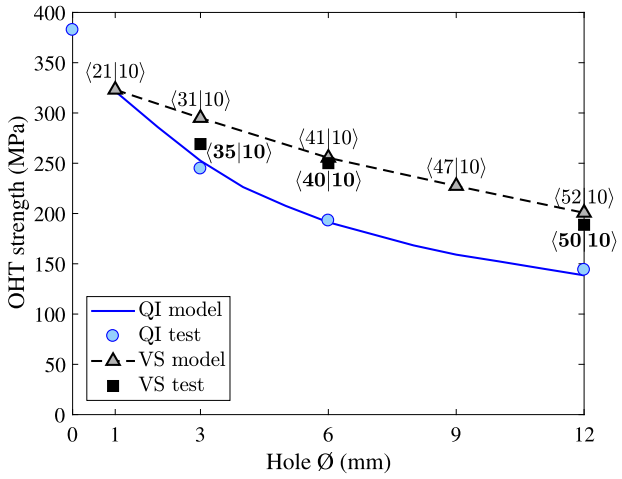

Fig. 12. Effect of hole size on OHT strength for QI and VS laminates. The $\langle T_0|T_1\rangle$ values in bold are the tested configurations, and those above the curve are the optimal configuration according to the calibrated homogenised model.

suited for the production of components with small geometric features. However, current commercial printers still have major limitations for fibre path planning, and the design must be adapted to meet manufacturing requirements. Despite these limitations, in the present work the steered-fibre layer was filled with up to 80% cCF/PA reinforced material.

With regard to modelling the laminate behaviour, we show that the PS criterion for ultimate failure prediction developed for traditional composites is applicable to 3D printed laminates, as shown in the results of the QI laminate for different hole sizes. The homogenisation of mechanical properties calculated for steered-fibre plies is valid for a pre-design of the VS laminate, but an accurate prediction of the laminate strength requires the development of an as-manufactured model, as discussed in Section 5. This is due to the effect of defects (unreinforced gaps and fibre discontinuity) caused by manufacturing constraints. The reason for the correct prediction of the models is the behaviour of the laminate, which is fibre-dominated, with little subcritical damage and delamination. This behaviour may result from the design of robust laminates, where the steered-fibre and straight-fibre layers are combined in a proper stacking sequence, reducing the effect of manufacturing defects and stiffening the weaker directions.

In summary, VS laminates showed higher strength than QI laminates for holes larger than ∅1 mm, increasing to more than 30% for holes of ∅6 mm or larger. This is because of a favourable redistribution of the load which relieves the central area of the hole and loads the edges, resulting in fracture even outside the hole. This behaviour is achieved with an orientation of the fibres at the edges T_1 aligned with the loading direction, and with an orientation of the fibres in the centre T_0 inclined to overcome the geometrical discontinuity produced by the hole. For a given width, the larger the hole, the greater the inclination of the fibre at the centreline T_0. In fact, an almost non-responsive behaviour to the presence of a central hole was observed for fibre orientations T_0 higher than 55°. In addition, the increase in strength combined with the decrease in stiffness causes the energy absorbed up to failure to increase greatly, even double, which is highly beneficial for notched applications such as structurally-critical notches and fastening holes.

This work is a contribution to the modelling, design, and manufacture of 3D printed composites, and a further step towards the use of 3D printing to manufacture high-performance functional components in real applications.

CRediT authorship contribution statement

M. Iragi: Conceptualization, Investigation, Methodology, Software, Visualization, Writing – original draft. **C. Pascual-González:** Investigation, Resources, Visualization. **A. Esnaola:** Investigation, Resources, Writing – review & editing. **U. Morales:** Investigation, Resources, Visualization. **J. Aurrekoetxea:** Conceptualization, Funding acquisition, Writing – review & editing. **C.S. Lopes:** Conceptualization, Funding acquisition, Methodology, Project administration, Software, Validation. **L. Aretxabaleta:** Conceptualization, Funding acquisition, Methodology, Project administration, Software, Supervision, Validation, Writing – review & editing.

Declaration of competing interest

The authors declare that they have no known competing financial interests or personal relationships that could have appeared to influence the work reported in this paper.

Data availability

Data will be made available on request.

Acknowledgements

This paper is dedicated to the memory of Cláudio S. Lopes. We are very fortunate to have met and collaborated with Cláudio. He inspired us to undertake the research, gave us exceptional advice during the course of the study, and always motivated and encouraged us to continue.

This work was supported by the Spanish Ministry of Science, Innovation and Universities (MCIU), the Spanish state Research Agency (AEI) and the European Regional Development Fund (FEDER) [RTI2018-094435-B-C31, RTI2018-094435-B-C33], and the Basque Government, Spain [IT1613-22].

Appendix. Multi-scale homogenisation

The micro-mechanic expressions of the semi-empirical Chamis model [36] to determine the five independent elastic properties of the cCF/PA raw material are:

$$\begin{aligned}
E_{11}^{\text{raw}} &= v_{\text{f}} E_{11}^{\text{f}} + (1 - v_{\text{f}}) E^{\text{m}} \\
E_{22}^{\text{raw}} &= \frac{E^{\text{m}}}{1 - \sqrt{v_{\text{f}}}(1 - \frac{E^{\text{m}}}{E_{22}^{\text{f}}})} \\
\nu_{12}^{\text{raw}} &= v_{\text{f}} \nu_{12}^{\text{f}} + (1 - v_{\text{f}}) \nu^{\text{m}} \\
G_{12}^{\text{raw}} = G_{13}^{\text{raw}} &= \frac{G^{\text{m}}}{1 - \sqrt{v_{\text{f}}}(1 - \frac{G^{\text{m}}}{G_{12}^{\text{f}}})} \\
G_{23}^{\text{raw}} &= \frac{G^{\text{m}}}{1 - \sqrt{v_{\text{f}}}(1 - \frac{G^{\text{m}}}{G_{23}^{\text{f}}})}
\end{aligned} \tag{A.1}$$

where the fibre and matrix properties are denoted by the superscript f and m, respectively. The behaviour of the thermoplastic matrix is considered isotropic in this model. The fibre volume v_{f} is determined by Eq. (2), and changes as a function of the transverse y-position. The elastic properties of the ply meso-structure are determined from the Rodriguez void-model equations, and adapted for the transversely isotropic material [35]:

$$\begin{aligned}
E_{11} &= (1 - \rho_1) E_{11}^{\text{raw}} \\
E_{22} &= (1 - \sqrt{\rho_1}) E_{22}^{\text{raw}} \\
\nu_{12} &= (1 - \rho_1) \nu_{12}^{\text{raw}} \\
G_{12} = G_{13} &= 2 \frac{(1 - \rho_1)(1 - \sqrt{\rho_1})}{(1 - \rho_1) + (1 - \sqrt{\rho_1})} G_{12}^{\text{raw}} \\
G_{23} &= (1 - \sqrt{\rho_1}) G_{23}^{\text{raw}}
\end{aligned} \tag{A.2}$$

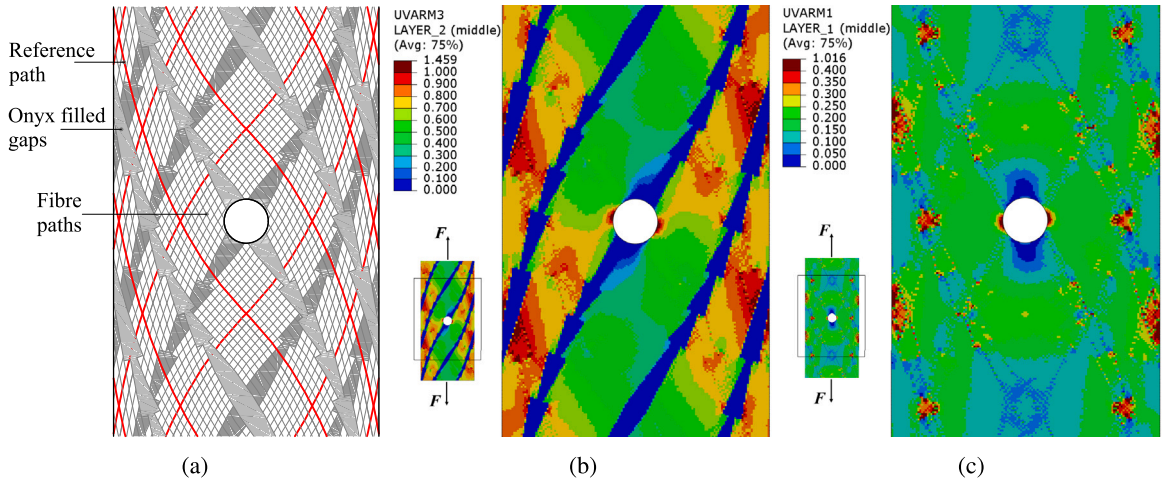

Fig. 13. As-manufactured modelling of the VS⟨45|10⟩ and ∅6 mm configuration: (a) Onyx-filled gaps and fibre paths of the two adjacent ±⟨45|10⟩ steered-fibre layers, (b) fibre tensile failure index field in the steered-fibre ply at ultimate failure state, and (c) matrix failure index field in the outer 45° ply at matrix failure onset state corresponding to 54% of the ultimate load.

The coefficient ρ_1 represents the void density in the plane perpendicular to direction 1 of the fibre or bead. ρ_1 was assigned the value of 7.5% based on experimental analysis of printed unidirectional cCF/PA samples in a previous work [13].

The homogenised tensile and compressive longitudinal strength properties of the printed cCF/PA meso-structure are shown in Eq. (A.3). These were determined with the Chamis model [38], which corresponds to the rule of mixtures. In the longitudinal direction, the contribution of the matrix was disregarded as the strength of the fibre dominates. The transverse and shear strength are matrix-dominated, and the influence of fibre content can be considered negligible for the range of fibre volume ratios of the material. Therefore, the transverse and shear strengths were considered to be those obtained in the experimental characterisation of the printed cCF/PA material [13], which are listed in Table 1.

$$X_T = (1-\rho_1)v_f X_T^f$$
$$X_C = (1-\rho_1)v_f X_C^f \quad \text{(A.3)}$$

The fibre and matrix effective properties required to apply the homogenisation model were predicted using reverse engineering from the experimental in-plane ply properties, and using the micro-mechanics and void-model equations. The predicted effective properties are set out in Table 3.

References

[1] C.S. Lopes, Z. Gürdal, P.P. Camanho, Tailoring for strength of composite steered-fibre panels with cutouts, Composites A 41 (12) (2010) 1760–1767, http://dx.doi.org/10.1016/j.compositesa.2010.08.011.

[2] A. Sabido, L. Bahamonde, R. Harik, M.J. van Tooren, Maturity assessment of the laminate variable stiffness design process, Compos. Struct. 160 (2017) 804–812, http://dx.doi.org/10.1016/j.compstruct.2016.10.081.

[3] H. Ghiasi, K. Fayazbakhsh, D. Pasini, L. Lessard, Optimum stacking sequence design of composite materials part II: Variable stiffness design, Compos. Struct. 93 (1) (2010) 1–13, http://dx.doi.org/10.1016/j.compstruct.2010.06.001.

[4] M.W. Hyer, H.H. Lee, The use of curvilinear fiber format to improve buckling resistance of composite plates with central circular holes, Compos. Struct. 18 (3) (1991) 239–261, http://dx.doi.org/10.1016/0263-8223(91)90035-W.

[5] Z. Gürdal, R. Olmedo, In-plane response of laminates with spatially varying fiber orientations - variable stiffness concept, AIAA J. 31 (4) (1993) 751–758, http://dx.doi.org/10.2514/3.11613.

[6] C.S. Lopes, P.P. Camanho, Z. Gürdal, B.F. Tatting, Progressive failure analysis of tow-placed, variable-stiffness composite panels, Int. J. Solids Struct. 44 (25) (2007) 8493–8516, http://dx.doi.org/10.1016/j.ijsolstr.2007.06.029.

[7] J. Frketic, T. Dickens, S. Ramakrishnan, Automated manufacturing and processing of fiber-reinforced polymer (FRP) composites: An additive review of contemporary and modern techniques for advanced materials manufacturing, Addit. Manuf. 14 (2017) 69–86, http://dx.doi.org/10.1016/j.addma.2017.01.003.

[8] O. Falcó, J.A. Mayugo, C.S. Lopes, N. Gascons, A. Turon, J. Costa, Variable-stiffness composite panels: As-manufactured modeling and its influence on the failure behavior, Composites B 56 (2014) 660–669, http://dx.doi.org/10.1016/j.compositesb.2013.09.003.

[9] P. Zhuo, S. Li, I.A. Ashcroft, A.I. Jones, Material extrusion additive manufacturing of continuous fibre reinforced polymer matrix composites: A review and outlook, Composites B 224 (2021) 109143, http://dx.doi.org/10.1016/j.compositesb.2021.109143.

[10] S. Yuan, S. Li, J. Zhu, Y. Tang, Additive manufacturing of polymeric composites from material processing to structural design, Composites B 219 (2021) 108903, http://dx.doi.org/10.1016/j.compositesb.2021.108903.

[11] U. Morales, A. Esnaola, M. Iragi, L. Aretxabaleta, J. Aurrekoetxea, The effect of cross-section geometry on crushing behaviour of 3D printed continuous carbon fibre reinforced polyamide profiles, Compos. Struct. 274 (2021) 114337, http://dx.doi.org/10.1016/j.compstruct.2021.114337.

[12] U. Morales, A. Esnaola, M. Iragi, L. Aretxabaleta, J. Aurrekoetxea, Quasi-static and dynamic crush behaviour of 3D printed thin-walled profiles reinforced with continuous carbon and glass fibres, Composites B 217 (2021) 108865, http://dx.doi.org/10.1016/j.compositesb.2021.108865.

[13] M. Iragi, C. Pascual-González, A. Esnaola, C.S. Lopes, L. Aretxabaleta, Ply and interlaminar behaviours of 3D printed continuous carbon fibre-reinforced thermoplastic laminates; Effects of processing conditions and microstructure, Addit. Manuf. 30 (2019) 100884, http://dx.doi.org/10.1016/j.addma.2019.100884.

[14] B. Brenken, E. Barocio, A. Favaloro, V. Kunc, R.B. Pipes, Fused filament fabrication of fiber-reinforced polymers: A review, Addit. Manuf. 21 (2018) 1–16, http://dx.doi.org/10.1016/j.addma.2018.01.002.

[15] Z. Hou, X. Tian, J. Zhang, Z. Zheng, L. Zhe, D. Li, A.V. Malakhov, A.N. Polilov, Optimization design and 3D printing of curvilinear fiber reinforced variable stiffness composites, Compos. Sci. Technol. 201 (2021) 108502, http://dx.doi.org/10.1016/j.compscitech.2020.108502.

[16] S. Khan, K. Fayazbakhsh, Z. Fawaz, M. Arian Nik, Curvilinear variable stiffness 3D printing technology for improved open-hole tensile strength, Addit. Manuf. 24 (2018) 378–385, http://dx.doi.org/10.1016/j.addma.2018.10.013.

[17] T. Suzuki, S. Fukushige, M. Tsunori, Load path visualization and fiber trajectory optimization for additive manufacturing of composites, Addit. Manuf. 31 (2020) 100942, http://dx.doi.org/10.1016/j.addma.2019.100942.

[18] R.T. Ferreira, I.A. Ashcroft, Optimal orientation of fibre composites for strength based on Hashin's criteria optimality conditions, Struct. Multidiscip. Optim. (2020) 1–22, http://dx.doi.org/10.1007/s00158-019-02462-w.

[19] T. Shafighfard, T.A. Cender, E. Demir, Additive manufacturing of compliance optimized variable stiffness composites through short fiber alignment along curvilinear paths, Addit. Manuf. 37 (2021) 101728, http://dx.doi.org/10.1016/j.addma.2020.101728.

[20] Y. Yamanaka, A. Todoroki, M. Ueda, Y. Hirano, R. Matsuzaki, et al., Fiber line optimization in single ply for 3D printed composites, Open J. Compos. Mater. 6 (04) (2016) 121, http://dx.doi.org/10.4236/ojcm.2016.64012.

[21] E. Zappino, M. Filippi, A. Pagani, M. Petiti, E. Carrera, Experimental and numerical analysis of 3D printed open-hole plates reinforced with carbon fibers, Compos. Part C: Open Access 2 (2020) 100007, http://dx.doi.org/10.1016/j.jcomc.2020.100007.

[22] H. Zhang, A.N. Dickson, Y. Sheng, T. McGrail, D.P. Dowling, C. Wang, A. Neville, D. Yang, Failure analysis of 3D printed woven composite plates with holes under tensile and shear loading, Composites B 186 (2020) 107835, http://dx.doi.org/10.1016/j.compositesb.2020.107835.

[23] N. Li, G. Link, T. Wang, V. Ramopoulos, D. Neumaier, J. Hofele, M. Walter, J. Jelonnek, Path-designed 3D printing for topological optimized continuous carbon fibre reinforced composite structures, Composites B 182 (2020) 107612, http://dx.doi.org/10.1016/j.compositesb.2019.107612.

[24] H. Zhang, A. Li, J. Wu, B. Sun, C. Wang, D. Yang, Effectiveness of fibre placement in 3D printed open-hole composites under uniaxial tension, Compos. Sci. Technol. 220 (2022) 109269, http://dx.doi.org/10.1016/j.compscitech.2022.109269.

[25] G.T. Mark, A.S. Gozdz, Apparatus for fiber reinforced additive manufacturing, 2014, US 2014/0328963 A1.

[26] Markforged Inc., Material datasheet - rev 4.0, 2020, URL https://markforged.com.

[27] C. Pascual-González, M. Iragi, A. Fernández, J.P. Fernández-Blázquez, L. Aretxabaleta, C.S. Lopes, An approach to analyse the factors behind the micromechanical response of 3D-printed composites, Composites B 186 (2020) 107820, http://dx.doi.org/10.1016/j.compositesb.2020.107820.

[28] M. Iragi, C. Pascual-González, A. Esnaola, J. Aurrekoetxea, C.S. Lopes, L. Aretxabaleta, Interlaminar fracture toughness of 3D printed continuous carbon fibre-reinforced polyamide / Tenacidad a la fractura interlaminar de poliamida reforzada con fibra de carbono continua impresa en 3D, Mater. Compuestos 4 (1) (2020) 67–71.

[29] C. Pascual-González, P. San Martín, I. Lizarralde, A. Fernández, A. León, C.S. Lopes, J.P. Fernández-Blázquez, Post-processing effects on microstructure, interlaminar and thermal properties of 3D printed continuous carbon fibre composites, Composites B 210 (2021) 108652, http://dx.doi.org/10.1016/j.compositesb.2021.108652.

[30] H. Shiratori, A. Todoroki, M. Ueda, R. Matsuzaki, Y. Hirano, Mechanism of folding a fiber bundle in the curved section of 3D printed carbon fiber reinforced plastics, Adv. Compos. Mater. 29 (3) (2020) 247–257, http://dx.doi.org/10.1080/09243046.2019.1682794.

[31] H. Zhang, J. Chen, D. Yang, Fibre misalignment and breakage in 3D printing of continuous carbon fibre reinforced thermoplastic composites, Addit. Manuf. 38 (2021) 101775, http://dx.doi.org/10.1016/j.addma.2020.101775.

[32] A. Catapano, M. Montemurro, J.-A. Balcou, E. Panettieri, Rapid prototyping of variable Angle-Tow composites, Aerotecnica Missili Spazio 98 (4) (2019) 257–271, http://dx.doi.org/10.1007/s42496-019-00019-0.

[33] ASTM International, ASTM D5766/D5766M-11: Standard Test Method for Open-Hole Tensile Strength of Polymer Matrix Composite Laminates, ASTM International, West Conshohocken, PA, 2018, http://dx.doi.org/10.1520/D5766_D5766M-11R18.

[34] Abaqus, Inc., ABAQUS/Standard User's Manual, Version 6.14, Dassault Systèmes Simulia Corp, United States, 2014.

[35] E. Polyzos, A. Katalagarianakis, D. Polyzos, D. Van Hemelrijck, L. Pyl, A multiscale analytical methodology for the prediction of mechanical properties of 3D-printed materials with continuous fibres, Addit. Manuf. 36 (2020) 101394, http://dx.doi.org/10.1016/j.addma.2020.101394.

[36] C.C. Chamis, Simplified composite micromechanics equations for hygral, thermal and mechanical properties, in: SAMPE Quarterly, Vol. 15, 1983.

[37] J.F. Rodríguez, J.P. Thomas, J.E. Renaud, Mechanical behavior of acrylonitrile butadiene styrene fused deposition materials modeling, Rapid Prototyp. J. (2003) http://dx.doi.org/10.1108/13552540310489604.

[38] C.C. Chamis, F. Abdi, M. Garg, L. Minnetyan, H. Baid, D. Huang, J. Housner, F. Talagani, Micromechanics-based progressive failure analysis prediction for WWFE-III composite coupon test cases, J. Compos. Mater. 47 (20–21) (2013) 2695–2712, http://dx.doi.org/10.1177/0021998313499478.

[39] D.D.L. Chung, CHAPTER 4 - properties of carbon fibers, in: D.D. Chung (Ed.), Carbon Fiber Composites, Butterworth-Heinemann, Boston, 1994, pp. 65–78, http://dx.doi.org/10.1016/B978-0-08-050073-7.50008-7.

[40] C.L. Pai, M. Boyce, G. Rutledge, Mechanical properties of individual electrospun PA 6(3)T fibers and their variation with fiber diameter, Polymer 52 (2011) 2295–2301, http://dx.doi.org/10.1016/j.polymer.2011.03.041.

[41] J. Gu, P. Chen, Extension of Puck's inter fibre fracture (IFF) criteria for UD composites, Compos. Sci. Technol. 162 (2018) 79–85, http://dx.doi.org/10.1016/j.compscitech.2018.04.019.

[42] T.A. Dutra, R.T.L. Ferreira, H.B. Resende, B.J. Blinzler, R. Larsson, Expanding Puck and Schürmann inter fiber fracture criterion for fiber reinforced thermoplastic 3D-printed composite materials, Materials 13 (7) (2020) http://dx.doi.org/10.3390/ma13071653.

[43] H. Tang, Q. Sun, Z. Li, X. Su, W. Yan, Longitudinal compression failure of 3D printed continuous carbon fiber reinforced composites: An experimental and computational study, Composites A 146 (2021) 106416, http://dx.doi.org/10.1016/j.compositesa.2021.106416.

[44] S.T. Pinho, R. Darvizeh, P. Robinson, C. Schuecker, P.P. Camanho, Material and structural response of polymer-matrix fibre-reinforced composites, J. Compos. Mater. 46 (19–20) (2012) 2313–2341, http://dx.doi.org/10.1177/0021998312454478.

[45] S.T. Pinho, G.M. Vyas, P. Robinson, Material and structural response of polymer-matrix fibre-reinforced composites: Part B, J. Compos. Mater. 47 (6–7) (2013) 679–696, http://dx.doi.org/10.1177/0021998313476523.

[46] S.T. Pinho, C.G. Dávila, P.P. Camanho, L. Iannucci, P. Robinson, Failure models and criteria for FRP under in-plane or three-dimensional stress states including shear non-linearity, 2005.

[47] P.P. Camanho, C.G. Dávila, S.T. Pinho, L. Iannucci, P. Robinson, Prediction of in situ strengths and matrix cracking in composites under transverse tension and in-plane shear, Composites A 37 (2) (2006) 165–176, http://dx.doi.org/10.1016/j.compositesa.2005.04.023, CompTest 2004.

[48] J.D. Santos, A. Fernández, L. Ripoll, N. Blanco, Experimental characterization and analysis of the in-plane elastic properties and interlaminar fracture toughness of a 3D-printed continuous carbon fiber-reinforced composite, Polymers 14 (3) (2022) http://dx.doi.org/10.3390/polym14030506.

[49] B.G. Green, M.R. Wisnom, S.R. Hallett, An experimental investigation into the tensile strength scaling of notched composites, Composites A 38 (3) (2007) 867–878, http://dx.doi.org/10.1016/j.compositesa.2006.07.008.

[50] P.P. Camanho, P. Maimí, C.G. Dávila, Prediction of size effects in notched laminates using continuum damage mechanics, Compos. Sci. Technol. 67 (13) (2007) 2715–2727, http://dx.doi.org/10.1016/j.compscitech.2007.02.005.

[51] J.M. Whitney, R.J. Nuismer, Stress fracture criteria for laminated composites containing stress concentrations, J. Compos. Mater. 8 (3) (1974) 253–265, http://dx.doi.org/10.1177/002199837400800303.

[52] P. Chen, Z. Shen, J.Y. Wang, Prediction of the strength of notched fiber-dominated composite laminates, Compos. Sci. Technol. 61 (9) (2001) 1311–1321, http://dx.doi.org/10.1016/S0266-3538(01)00030-6.